Topotactically constructed nickel-iron (oxy)hydroxide with abundant in-situ produced high-valent iron species for efficient water oxidation

Zhichong Kuang, Song Liu, Xuning Li, Meng Wang, Xinyi Ren, Jie Ding, Rile Ge, Wenhui Zhou, Alexandre Rykov, Moulay Tahar Sougrati, et al.

Journal Pre-proofs

Topotactically constructed nickel-iron (oxy)hydroxide with abundant *in-situ* produced high-valent iron species for efficient water oxidation

Zhichong Kuang, Song Liu, Xuning Li, Meng Wang, Xinyi Ren, Jie Ding, Rile Ge, Wenhui Zhou, Alexandre I. Rykov, Moulay T. Sougrati, Pierre-Emmanuel Lippens, Yanqiang Huang, Junhu Wang

PII: S2095-4956(20)30649-5
DOI: https://doi.org/10.1016/j.jechem.2020.09.014
Reference: JECHEM 1596

To appear in: *Journal of Energy Chemistry*

Received Date: 16 August 2020
Revised Date: 10 September 2020
Accepted Date: 15 September 2020

Please cite this article as: Z. Kuang, S. Liu, X. Li, M. Wang, X. Ren, J. Ding, R. Ge, W. Zhou, A.I. Rykov, M.T. Sougrati, P-E. Lippens, Y. Huang, J. Wang, Topotactically constructed nickel-iron (oxy)hydroxide with abundant *in-situ* produced high-valent iron species for efficient water oxidation, *Journal of Energy Chemistry* (2020), doi: https://doi.org/10.1016/j.jechem.2020.09.014

Topotactically constructed nickel-iron (oxy)hydroxide with abundant *in-situ* produced high-valent iron species for efficient water oxidation

Zhichong Kuang[a,b,c], Song Liu[b,d], Xuning Li[a,d,g], Meng Wang[e], Xinyi Ren[b,d], Jie Ding[d], Rile Ge[a,c], Wenhui Zhou[a,c], Alexandre I. Rykov[a,c], Moulay T. Sougrati[f], Pierre-Emmanuel Lippens[f], Yanqiang Huang[d], Junhu Wang[a,c,*]

[a]*Center for Advanced Mössbauer Spectroscopy, Dalian Institute of Chemical Physics, Chinese Academy of Sciences, Dalian 116023, Liaoning, China*
[b]*University of Chinese Academy of Sciences, Beijing 100049, China*
[c]*State Key Laboratory of Catalysis, Dalian Institute of Chemical Physics, Chinese Academy of Sciences, Dalian 116023, Liaoning, China*
[d]*CAS Key Laboratory of Science and Technology on Applied Catalysis, Dalian Institute of Chemical Physics, Chinese Academy of Sciences, Dalian 116023, Liaoning, China*
[e]*Department of Chemistry and Biotechnology, School of Engineering, Nagoya University, Nagoya 464-8601, Japan*
[f]*Institut Charles Gerhard, UMR 5253, CNRS, Université de Montpellier, Place Eugène Bataillon, 34095 Montpellier Cedex 5, France*
[g]*Nanyang Technological University, Singapore 637459, Singapore*

[*]Corresponding author. *E-mail address:* wangjh@dicp.ac.cn (J. Wang).

Abstract

The low efficiency of oxygen evolution reaction (OER) is regarded as one of the major roadblocks for metal-air batteries and water electrolysis. Herein, a high-performance OER catalyst of $NiFe_{0.2}$ (oxy)hydroxide ($NiFe_{0.2}$-O_xH_y) was developed through topotactic transformation of a Prussian blue analogue in an alkaline solution, which exhibits a low overpotential of only 263 mV to reach a current density of 10 mA cm^{-2} and a small Tafel slope of 35 mV dec^{-1}. *Ex-situ*/*operando* Raman spectroscopy results indicated that the phase structure of $NiFe_{0.2}$-O_xH_y was irreversibly transformed from the type of α-$Ni(OH)_2$ to γ-NiOOH with applying an anodic potential, while *ex-*

situ/*operando* ^{57}Fe Mössbauer spectroscopic studies evidenced the *in-situ* production of abundant high-valent iron species under OER conditions, which effectively promoted the OER catalysis. Our work elucidates that the amount of high-valent iron species *in-situ* produced in the NiFe (oxy)hydroxide has a positive correlation with its water oxidation reaction performance, which further deepens the understanding of the mechanism of NiFe-based electrocatalysts.

Keywords: Oxygen evolution reaction; Topotactic construction; Structural transformation; *Operando* Mössbauer spectroscopy; High-valent iron ion

1. Introduction

Oxygen evolution reaction (OER), as a core reaction in water electrolysis and for the storage of renewable electricity, has received lots of research attentions over the past few years [1–4]. The development of low-cost and high-efficiency OER catalysts with low overpotential and high stability is of great significance for the renewable energy technologies [5–8].

Among the various studied low-cost OER catalysts, NiFe-based (oxy)hydroxide materials show excellent catalytic activities [9–15]. Previous studies have evidenced that the water oxidation is usually proceeded *via* the nucleophilic attack of water molecule or hydroxide ions on the high-valent Fe or Ni center (such as Fe^{4+} or Ni^{4+}) over NiFe (oxy)hydroxides during OER [16–19]. For instance, Stahl et al. discovered that the NiOOH lattice could promote the formation of Fe^{4+} and experimentally evidenced the existence of Fe^{4+} using *ex-situ*/*operando* ^{57}Fe Mössbauer spectroscopy under OER conditions [17]. Density functional theory (DFT) calculations performed by Goldsmith and co-workers confirmed the critical role of NiOOH lattice for boosting the oxidation of Fe^{3+} to Fe^{4+} [20]. However, up to know, the real active center and the role of Fe^{4+} in NiFe-based (oxy)hydroxide for OER are still under debate.

In this work, a series of $NiFe_m$ (oxy)hydroxide ($NiFe_m$-O_xH_y, *m* refers to the atomic ratio of Fe/Ni) catalysts were synthesized by the topotactic transformation of $NiFe_m$-Fe Prussian blue analogues (PBAs) in an alkaline solution. An optimized OER catalytic performance with a low overpotential of 263 mV and a small Tafel slope of 35 mV dec^{-1} at the current density of 10 mA cm^{-2} in 1.0 M KOH aqueous solution was achieved over the optimized $NiFe_{0.2}$-O_xH_y, which is superior to the state-of-the-art RuO_2 catalyst. *Ex-situ*/*operando* Raman spectroscopy results showed that the phase structure of $NiFe_{0.2}$-O_xH_y was irreversibly converted from the type of α-$Ni(OH)_2$ to γ-NiOOH under an applied anodic potential. Furthermore, *ex-situ*/*operando* Mössbauer spectroscopy measurements evidenced the *in-situ* production of abundant high-valent iron species near the OER onset potential. A positive correlation between the amount of the high-valent iron ions and the OER activities at various applied potentials was observed in the first time, which is vitally useful to insight into the catalyzing mechanism of the water oxidation reaction over NiFe-based (oxy)hydroxide electrocatalysts.

2. Experimental

2.1. Materials

Ferrous chloride and nickel nitrate were purchased from Tianjin Daomao Chemical Reagent Co., Ltd., China. Potassium hexacyanocobaltate(III) (98%) was purchased from Beijing J&K Co., Ltd., China. Potassium chloride (99%) and potassium hydroxide (95%) were purchased from Sigma-Aldrich. Nafion solution (5 wt%) was obtained from Alfa Aesar. All chemical reagents were used without further purification.

2.2. Sample preparation

2.2.1 Preparation of $NiFe_m$-Fe PBAs, m = 0.11, 0.20, 0.25, 0.29

$NiFe_m[Fe(CN)_6]_{m+(2/3)}$ ($NiFe_m$-Fe PBAs, *m* = 0.11, 0.20, 0.25, 0.29) was prepared by a coprecipitation method [21]. It is described here that the synthesis process of

$NiFe_{0.20}$-Fe PBA, the other samples are prepared by the same method, except for changing the different Fe/Ni molar ratios. Briefly, 987.8 mg of $K_3[Fe(CN)_6]$ was dissolved in 300 mL ultrapure water (18.2 MΩ) in a 500 mL beaker (solution A with 10 M concentration). Meanwhile, 822.8 mg of $NiCl_2 \cdot 6H_2O$ and 187.1 mg of $FeCl_3$ were dissolved in 600 mL ultrapure water in a 1 L beaker (solution B with 11.5 M $NiCl_2 \cdot 6H_2O$ and 2.3 M $FeCl_3 \cdot 6H_2O$). Then solution A was dropwise added into solution B, followed by stirring for 30 min and aging for 20 h. Finally, the produced precipitates were centrifuged and washed at least three times using ultrapure water and then dried at 333 K in an electric oven for 12 h.

2.2.2 Preparation of $NiFe_m$-O_xH_y electrocatalysts, m = 0.11, 0.20, 0.25, 0.29

Like the reason in the previous section, the preparation of $NiFe_m$-O_xH_y electrocatalysts (m = 0.11, 0.20, 0.25, 0.29) was explained by that of $NiFe_{0.2}$-O_xH_y. 200 mg of $NiFe_{0.2}$-Fe PBA was suspended in 100 mL ultrapure water, followed by adding 200 mL 2 M KOH aqueous solution under vigorous stirring. 15 min later, the product was centrifuged and washed with ultrapure water several times and dried in vacuum oven for 20 h.

2.3. Conventional characterization techniques

The structure of the as-prepared catalysts was characterized by X-ray diffraction (XRD) on a PANalytical X'Pert-Pro X-ray diffractometer with Ni-filtered Cu K_α (λ = 0.1154 nm) radiation source. The X-ray photoelectron spectroscopy (XPS) measurements were performed on an ESCALAB 250 X-ray photoelectron spectroscope with monochromatic Al Kα radiation. All binding energies were calibrated by a standard sample of carbon (C 1*s* = 284.8 eV). High-resolution transmission electron microscopy (HRTEM), selected area electron diffraction (SAED), and energy dispersive X-ray spectroscopy (EDX) measurements were conducted on a JEOL

JEMARM200F. The Fe/Ni content were quantified by inductively coupled plasma optical emission spectroscopy (ICP-OES; ICPS-8100, Shimadzu).

2.4. Electrochemical measurements

All OER activities of $NiFe_m$-O_xH_y were performed on a typical three-electrode cell, which used a rotating disk electrode (RDE) (Pine Instrument Company, at a rotation speed of 1600 rpm) with a CHI 660E electrochemical workstation at ambient temperature. The graphite rod (diameter, 6 mm) and saturated calomel electrode (saturated potassium chloride solution) was used as the counter and reference electrodes, respectively. Glassy carbon electrode (5 mm diameter, 0.196 cm^2) coated with catalyst was used as the working electrode. To prepare the working electrode, carbon nanotubes treated by acid were mixed with the as-prepared catalyst to increase the conductivity (8 wt%). About 4 mg of the catalyst was added into 1 mL of Nafion solution (5 wt%), and sonicated for at least 6 h to obtain the catalyst ink. Then the catalyst ink was drop-casted onto the glassy carbon electrode with a mass loading of 0.20 mg cm^{-2}, and dried naturally in air. 1.0 M KOH aqueous solution was used as the electrolyte and all electrochemical experiments were carried out at room temperature.

The Ni foam supported with the $NiFe_{0.2}$-O_xH_y as working electrode to prevent the catalyst from falling off electrode at large current density in stability testing. In stability test, graphite rod (diameter, 6 mm) and saturated calomel electrode (saturated potassium chloride solution) also was used as the counter and reference electrodes, respectively, and the catalyst ink was drop-dried onto Ni foam (thickness, 0.34 mm) as working electrode.

All potentials were converted to the reversible hydrogen electrode (RHE) scale according to the following Nernst equation Eq. (1). Before electrochemical test, the as-prepared electrode was activated via cyclic voltammetry at a scan rate of 10 mV s^{-1}.

$$E_{(\text{vs. RHE})} = E_{(\text{vs. SCE})} + 0.0591 \times pH + 0.241 \quad (1)$$

2.5. Ex-situ/operando Raman and ^{57}Fe Mössbauer characterization techniques

The *ex-situ/operando* Raman spectra were collected on a Renishaw InVia microprobe Raman spectrometer with a 532 nm excitation laser. A self-developed *in-situ/operando* Raman characterization cell was used for the operando measurements as shown in Fig. S1. During the *operando* measurements, Ag/AgCl electrode and platinum wire were used as reference and counter electrodes, respectively. The potentials were converted to the reversible hydrogen electrode (RHE) scale according to Eq. (2). The prepared $NiFe_{0.2}$-O_xH_y catalyst inks were separately drop-dried onto a 1.0 cm × 2.0 cm glassy carbon sheet as work electrode.

$$E_{(\text{vs. RHE})} = E_{(\text{vs. Ag/AgCl})} + 0.0591 \times pH + 0.197\ \text{V} \quad (2)$$

The *ex-situ/operando* ^{57}Fe Mössbauer spectra were recorded using a proportional counter and a Topologic 500A spectrometer with ^{57}Co(Rh) as a γ-ray radioactive source. The spectra were fitted by using the MossWinn 4.0 program, and ^{57}Fe isomer shift values were given relative to α-iron as a standard. *The operando* Mössbauer spectroscopy measurements were performed on a set of self-developed *operando* electrochemical ^{57}Fe Mössbauer instrument as schematically shown in Scheme 1 and Fig. S2, which can be applied for dynamically observe the evolution of chemical state of the iron in the catalyst during electrochemical reactions. During the *operando* measurements, the prepared $NiFe_{0.2}$-O_xH_y catalyst ink was evenly coated on the carbon paper as work electrode, Ag/AgCl electrode and platinum wire were used as the reference and counter electrodes, respectively.

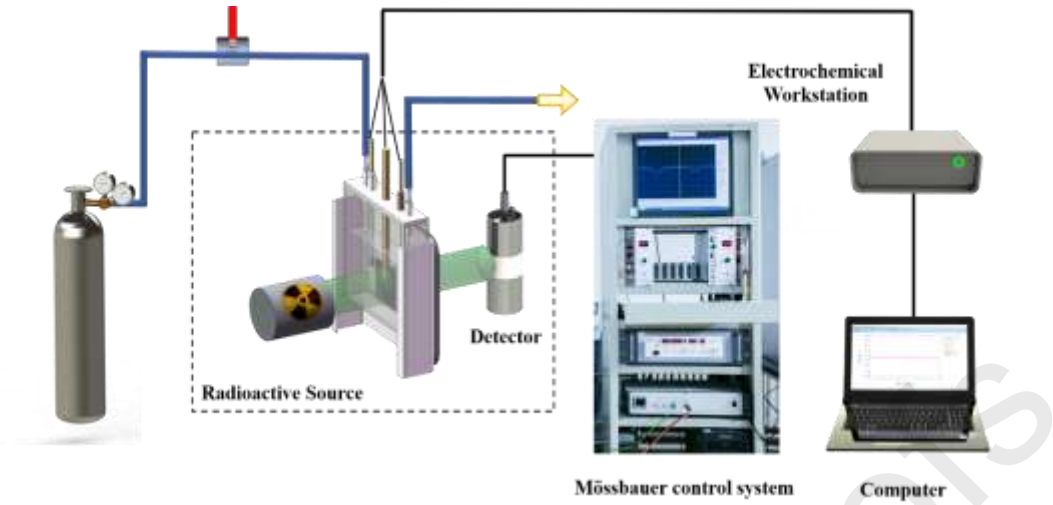

Scheme 1. The self-developed operando electrochemical ^{57}Fe Mössbauer instrument.

3. Results and discussion

3.1. Structure of the catalyst

As described above, the $NiFe_m$ (oxy)hydroxides ($NiFe_m$-O_xH_y, *m* refers to the molar ratio of Fe/Ni) were prepared by the topotactic transformation of $NiFe_m$-Fe PBAs ($NiFe_m[Fe(CN)]_{(m+2/3)}$) precursors in the 2 M KOH alkaline solution. The precursors of $NiFe_m$-Fe PBAs were prepared by the reported coprecipitation method [18]. As displayed in Fig. 1(a), the XRD patterns show the major diffraction peaks of $NiFe_m$-Fe PBAs, which match well with that of $Ni_3[Fe(CN)_6]_2 \cdot 10H_2O$ (JCPDS No. 46-0906), indicating pure phase of $NiFe_m$-Fe PBAs were prepared with Ni^{2+} partially replaced by Fe^{3+}. After separately immersing the series of $NiFe_m$-Fe PBAs in the alkaline solution, the $NiFe_m$-Fe PBAs were topotactically converted to $NiFe_m$-O_xH_y with low crystallinity (Fig. 1b) [22].

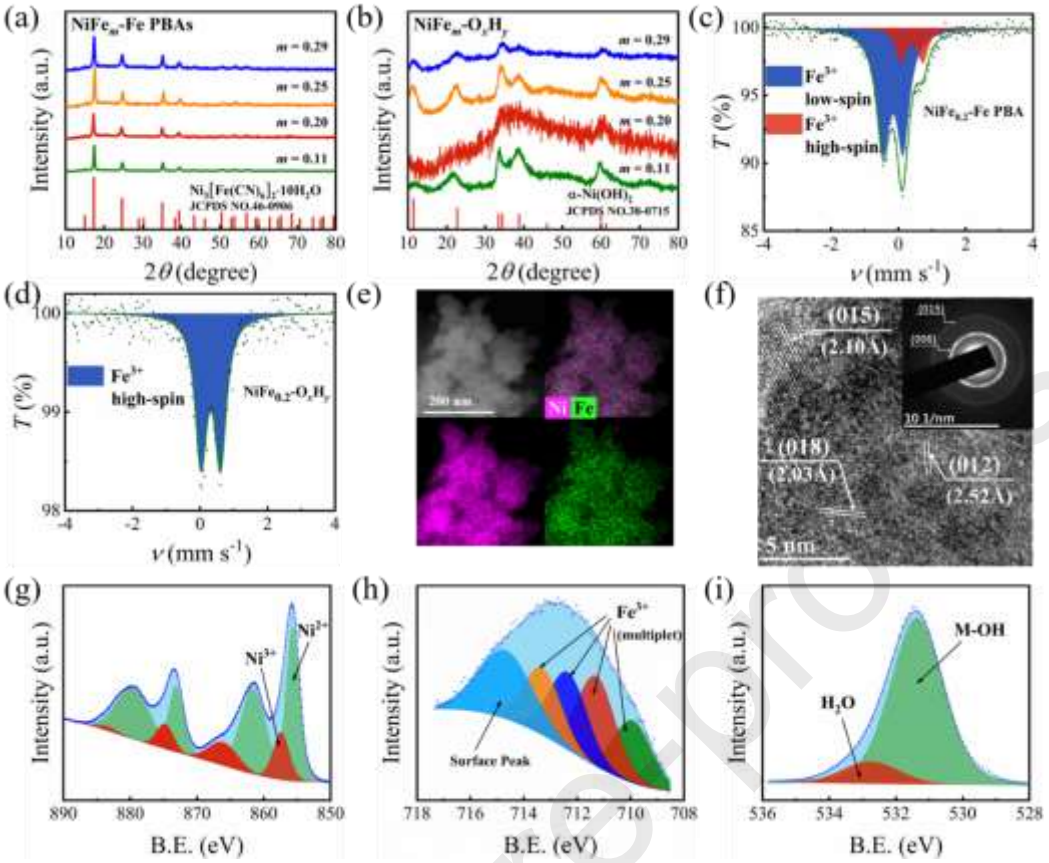

Fig. 1. XRD patterns of (a) NiFe$_m$-Fe PBAs and (b) NiFe$_m$-O$_x$H$_y$ with different molar ratios of Fe/Ni. *Ex-situ* ^{57}Fe Mössbauer spectra of (c) NiFe$_{0.2}$-Fe PBA and (d) NiFe$_{0.2}$-O$_x$H$_y$. (e) TEM image, corresponding EDX elemental mappings and (f) HRTEM image of NiFe$_{0.2}$-O$_x$H$_y$. The inset shows the SAED patterns of NiFe$_{0.2}$-O$_x$H$_y$. XPS spectra of (g) Ni 2*p*, (h) Fe 2*p*, and (i) O 1*s* for NiFe$_{0.2}$-O$_x$H$_y$.

Ex-situ ^{57}Fe Mössbauer spectroscopic measurements were conducted to study the chemical states of Fe in the as-prepared NiFe$_m$-O$_x$H$_y$ catalysts. As shown in Fig. 1(c) and Fig. S3(a–c), *ex-situ* ^{57}Fe Mössbauer spectra of NiFe$_m$-Fe PBAs was observed (*m* = 0.11, 0.20, 0.25, 0.29), which has two kinds of Fe^{3+} [23–25]. Since C is stronger electron donor than N in the cyanogroup (CN^-), the Fe^{3+} in the $[Fe(CN)_6]^{3+}$ large anions is low spin state while the Fe^{3+} that replaced the partial Ni^{2+} outside $[Fe(CN)_6]^{3+}$ is in the high spin state [26–28], which was clearly confirmed by *ex-situ* Mössbauer characterization of NiFe$_m$-Fe PBAs. In the meanwhile, with the increase of Fe doping

amount, the proportion of high spin Fe^{3+} also increases gradually (Table S1), which also further indicates the successful doping of Fe with different content. After immersed in 2 M KOH aqueous solution, the shoulder absorption peaks in the Mössbauer spectra of NiF_m-Fe PBAs corresponding to $[Fe(CN)_6]^{3-}$ was disappeared, indicating that the $NiFe_m$-Fe PBAs has been completely destructed and transformed into $NiFe_m$-O_xH_y (Fig. 1d and Fig. 3Sd–f)), which is well consistent with the XRD results (Fig. 1b).

Fig. 1(e) displays a TEM image and the corresponding EDX elemental mappings of the selected $NiFe_{0.2}$-O_xH_y, which shows uniform distributions of Ni and Fe. The observed interplanar spacings of 2.03, 2.10 and 2.52 Å from the HRTEM image can be assigned to the (015), (018) and (012) planes of the crystal structure α-$Ni(OH)_2$ (Fig. 1f), respectively [29], suggesting the distribution of Fe species in the lattice of α-$Ni(OH)_2$. Additionally, the crystal planes of (015) and (006) from α-$Ni(OH)_2$ are clearly observable in the SAED patterns (inset in Fig. 1f), which is well consistent with the results of Mössbauer spectrum (Fig. 1d) and further demonstrates that the precursor $NiFe_{0.2}$-Fe PBA has been fully converted to $NiFe_{0.2}$-O_xH_y after being immersed in the alkaline solution.

The surface composition and valence states of $NiFe_m$-O_xH_y were analyzed by the XPS technique. Table S2 lists the binding energies of Ni 2*p*, Fe 2*p*, O 1*s* and N 1*s* obtained from XPS spectra of the selected $NiFe_{0.2}$-O_xH_y and $NiFe_{0.2}$-Fe PBA. All binding energies were calibrated by a standard sample of carbon (C 1*s* = 248.8 eV). As shown in Fig. 1(g), the peaks at 855.6 and 857.4 eV of Ni 2*p* for $NiFe_{0.2}$-O_xH_y can be assigned to Ni^{2+} and Ni^{3+}, respectively. As shown in Fig. S4(a), apart from Ni^{II}, Ni^{III} was also observed in the Ni 2*p* XPS spectrum of $NiFe_{0.2}$-Fe PBA, which can be explained as PBAs are unstable under X-ray irradiation and then Ni^{II} was partially oxidized into Ni^{III} on the surface of $NiFe_{0.2}$-Fe PBA [30,31]. Compared to the Fe 2*p*

XPS spectrum for $NiFe_{0.2}$-Fe PBA (Fig. S4b), a broad spectral band of that for $NiFe_{0.2}$-O_xH_y was observed (Fig. 1h), suggesting presence of multiple Fe species as previously reported by several groups [32,33]. The Fe 2*p* spectrum for $NiFe_{0.2}$-Fe PBA (Fig. S4b) indicates the presence of low spin Fe^{III} which is bonded to C of cyanogroup (Fe^{III}–CN) and high spin Fe^{III} bonded to N of cyanogroup (Fe^{III}–NC) which has a higher binding energy than Fe^{III}–CN [34]. This is consistent with the analysis of the *ex-situ* ^{57}Fe Mössbauer spectrum shown in Fig. 1(c). In addition, the observed Fe^{II} in the XPS spectrum of $NiFe_{0.2}$-Fe PBA (Fig. S4b) can be reasonably explained as that Fe^{III} was partially reduced under X-ray irradiation [31].

The O 1*s* peak of XPS spectrum of $NiFe_{0.2}$-O_xH_y was observed significantly shifted to lower binding energies as compared to that of $NiFe_{0.2}$-Fe PBA (Fig. S5a). The main peak at 531.4 eV can be attributed to M(Ni,Fe)–OH and the small peak at binding energy of 532.8 eV can be assigned to coordinated water (Fig. 1i) [32,35]. The high intensity of the M(Ni,Fe)–OH peak convincingly demonstrates that $NiFe_{0.2}$-O_xH_y was formed after the alkali treatment, which is consistent with the results of other characterizations. As shown in Fig. S5(a), down, the main O 1*s* peak at 532.5 eV and the small O 1*s* peak at 529.9 eV for $NiFe_{0.2}$-Fe PBA should be assigned to the water of crystallization and the very weak oxidation of the surface layer to Ni(Fe)-oxides, respectively [31].

The peaks observed at the binding energies of the N 1*s* XPS spectra of $NiFe_{0.2}$-O_xH_y centered at 398.0 eV and $NiFe_{0.2}$-Fe PBA centered at 398.2 eV can be assigned to cyanogroup (Fig. S5b) [31]. The N 1*s* peak of $NiFe_{0.2}$-O_xH_y is much weaker than that of $NiFe_{0.2}$-Fe PBA, indicating there are few residual $[Fe(CN)_6]^{3-}$ large anions at the surface of $NiFe_{0.2}$-O_xH_y. This also demonstrates that the $[Fe(CN)_6]^{3-}$ of $NiFe_{0.2}$-Fe PBA was almost dissociated after topotactically construction by anions exchange, which then

generated $NiFe_{0.2}$-O_xH_y. It is in accordance with the results obtained by ^{57}Fe Mössbauer spectroscopy and XRD.

3.2. Electrocatalytic performance for OER

The electrocatalytic performances of $NiFe_m$-O_xH_y for OER were assessed by linear sweep voltammetry (LSV) in 1.0 M KOH aqueous solution at a scan rate of 1 mV s^{-1} with iR correction (Fig. 2a) after electrochemical activation (Fig. S6). As shown in Fig. 2(a), the OER activity could be modulated by rational changing the molar ratio of Fe/Ni in $NiFe_m$-O_xH_y. As plotted in Fig. 2(b and c), an optimized catalytic performance with a low overpotential of 263 mV at the current density of 10 mA cm^{-2} and a small Tafel slope of 35 mV dec^{-1} was achieved over $NiFe_{0.2}$-O_xH_y, which is superior to the state-of-the-art RuO_2 catalyst with a overpotential potential of 288 mV at the same current density of 10 mA cm^{-2} with a Tafel slope of 55 mV dec^{-1}. In addition, the catalytic stability of $NiFe_{0.2}$-O_xH_y was also examined using the chronopotentiometry method. As shown in Fig. 2(d), the time-dependent potential curves were recorded at a large current density of 100 mA cm^{-2} on Ni foam (thickness, 0.34 mm) with different catalyst loading amounts (0.16, 0.23 mg cm^{-2}) showing no significant activity decay of $NiFe_{0.2}$-O_xH_y over 100 h of continuous reaction and the inset shows chronopotentiometric curves of $NiFe_{0.2}$-O_xH_y supported on a glass carbon electrode (diameter, 5 mm) at a constant current density of 10 mA cm^{-2}, which all indicate that $NiFe_{0.2}$-O_xH_y has a very good stability.

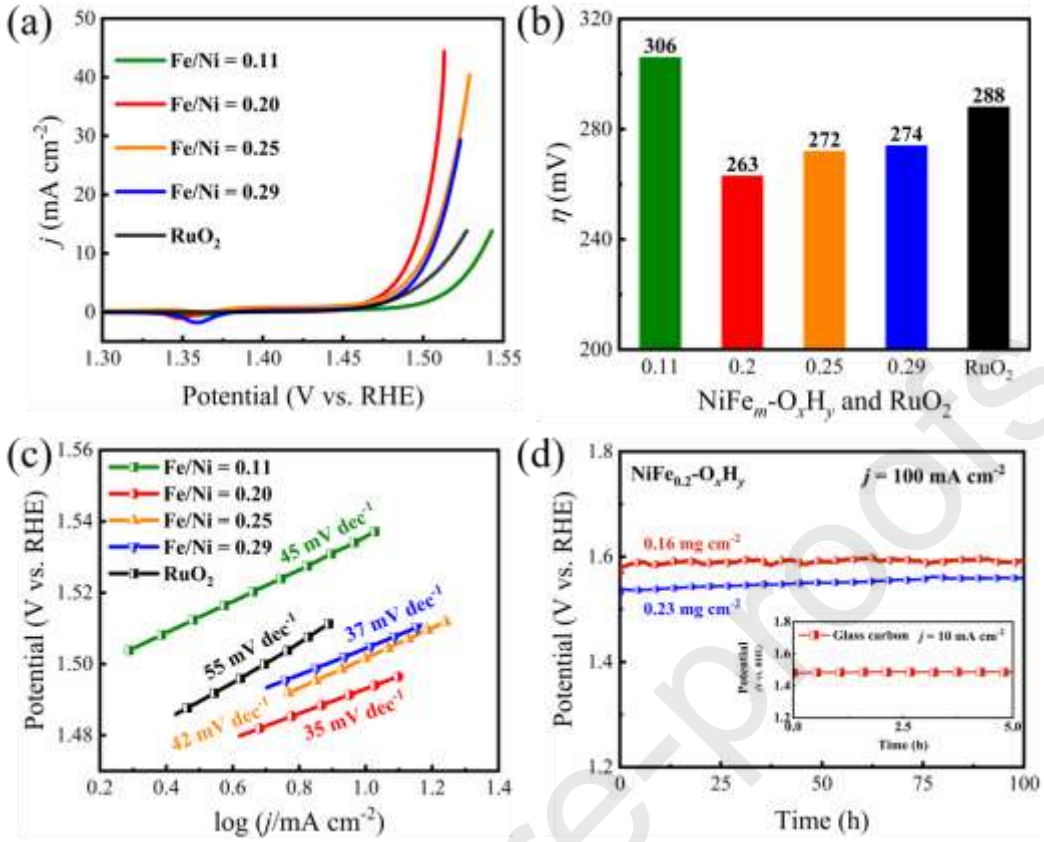

Fig. 2. (a) The OER polarization curves with iR correction. (b) Overpotentials at 10 mA cm^{-2} and (c) Tafel plots of $NiFe_m$-O_xH_y with different molar ratios of Fe/Ni and commercial RuO_2. (d) Chronopotentiometric curves of $NiFe_{0.2}$-O_xH_y on Ni foam (thickness, 0.34 mm) with different catalyst loading (0.16, 0.23 mg cm^{-2}) at a constant current density of 100 mA cm^{-2} for 100 h. The inset shows chronopotentiometric curves of $NiFe_{0.2}$-O_xH_y supported on a glass carbon electrode (diameter, 5 mm) at a constant current density of 10 mA cm^{-2}

3.3. Operando Raman and ^{57}Fe Mössbauer spectroscopic characterizations

To investigate the real active phase of $NiFe_m$-O_xH_y in OER, firstly, *ex-situ* Raman spectroscopy was performed (Fig. 3a and Fig. S7). As shown in Fig. 3(a), $NiFe_{0.2}$-O_xH_y has two Raman bands at 463 and 530 cm^{-1}, with the intensity of the band at 530 cm^{-1} stronger than that of 463 cm^{-1}, which is well consistent with that of the type of *α*-$Ni(OH)_2$ structure which has low Raman scattering cross-section [36–38]. After

electrochemical activation, both bands of $NiFe_{0.2}$-O_xH_y underwent an irreversible change and the intensity of the band at 476 cm^{-1} was obviously stronger than that of the band at 559 cm^{-1}. It is assigned to γ-NiOOH because of resonance Raman enhancement of γ-NiOOH [39]. Concurrently, the band intensities greatly increased, indicating a phase transformation from the phase structure of α-$Ni(OH)_2$ to γ-NiOOH [36,38]. Meanwhile, Fig. S6 shows the electrochemical activation curves of $NiFe_{0.2}$-O_xH_y for 100 cycles and cyclic voltammetry curves of $NiFe_{0.2}$-O_xH_y before (black curves) and after the electrochemical activation (red curves), and these results also imply the phase transformation of $NiFe_{0.2}$-O_xH_y during electrochemical activation.

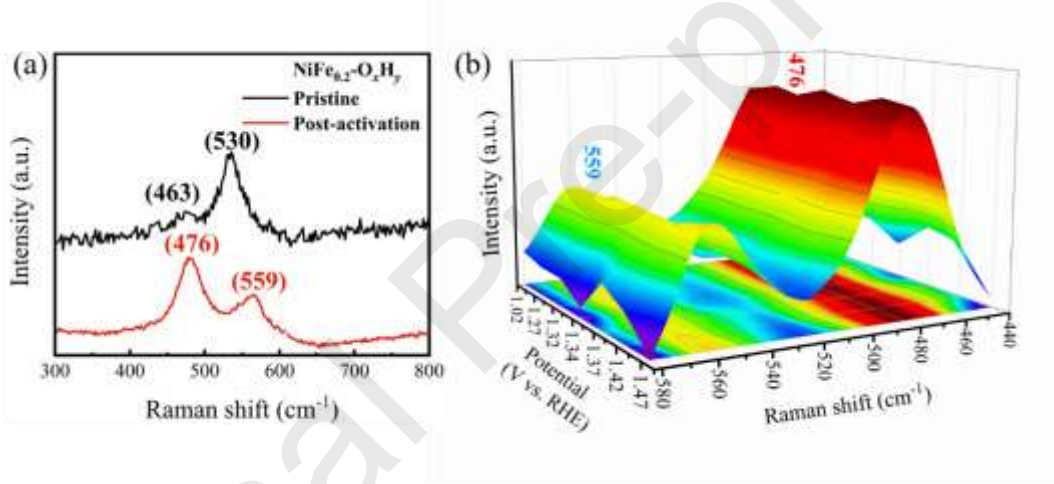

Fig. 3. (a) Raman spectra of $NiFe_{0.2}$-O_xH_y before (black) and after (red) applying anodic potential. (b) *Operando* Raman spectra of $NiFe_{0.2}$-O_xH_y collected at different applied potentials (V vs. RHE).

Operando Raman measurements were conducted to further study the evolution of crystal phase of γ-NiOOH in the selected $NiFe_{0.2}$-O_xH_y during OER. Negligible changes could be observed for the bands at 476 and 559 cm^{-1} when increasing the applied potentials from 1.02 to 1.47 mV (vs. RHE) (Fig. 3b), illustrating that the crystal phase of γ-NiOOH was stable and the phase transformation was irreversible. Based on previous theoretical studies, NiOOH has been considered as ineffective to produce O

radical [17]. However， the Ni^{3+} ions in Fe-doped γ-NiOOH could be increased the electron donating ability of bridging oxygen atoms, thus providing a stable environment for the *in-situ* production high valence state irons for the generation of active O intermediates [17,20].

Operando ^{57}Fe Mössbauer spectroscopy measurements were carried out to further investigate the evolution of Fe species in the selected $NiFe_{0.2}$-O_xH_y during OER. Negligible change was observed in the isomer shift value of $NiFe_{0.2}$-O_xH_y before and after electrochemical activation (Fig. S8), indicating that the valence state (Fe^{3+}) and spin state (high spin) of Fe^{3+} in $NiFe_{0.2}$-O_xH_y are the same before and after the electrochemical activation. The quadrupole splitting value of Fe^{3+} was observed smaller than the one before activation (Table S3), indicating that a more regular geometry of Fe^{3+} in the γ-phase NiOOH structure than that of the α-phase $Ni(OH)_2$ structure.

As shown in Fig. S9(a and b), the *operando* ^{57}Fe Mössbauer spectra of $NiFe_{0.2}$-O_xH_y collected at 1.22 V and 1.32 V (vs. RHE) are almost the same as the one collected at the open circuit voltage (Fig. 4a), and only one doublet is observed which is attributed to high spin Fe^{3+}. However, a small shoulder peak with a isomer shift value of -0.25 mm s^{-1} starts to develop (Fig. 4b) at an applied potential of 1.37 V (vs. RHE), which is attributed to the Fe^{4+} [17,24]. The content of Fe^{4+} further increases as the applied anode potential increases (Fig. 4c, d and Fig. S9c). What's more, the content of Fe^{4+} reaches ~40% (Fig. 4e) at 1.57 V (vs. RHE). Then the Fe^{4+} completely disappears after removing the applied potential (Fig. 4f), reflecting the critical role of Fe^{4+} species in OER. In the meantime, there was little change in the current during *operando* Mössbauer spectroscopy measurements (Fig. 4g and Fig. S10), which also indicates $NiFe_{0.2}$-O_xH_y has a good stability in OER. In combination with the cyclic voltammetry curves (Fig. 4h), it's clear that there's already a lot of Fe^{4+} (~12% in total iron ions)

being generated at around the OER onset (Fig. 4c), and Ni/Fe magnetic moment experiments also suggest that Fe^{3+} is more feasible to be oxidized to a higher oxidation [40]. It is different from previous tests, in which Fe^{4+} was observed at a higher potential rather than around onset potential (Table S4) [17].

Moreover, the *in-situ* production of abundant Fe^{4+} near the OER onset potential, combining with the positive correlation between the Fe^{4+} content and electric current under different applied potential (Fig. 4i), further proved the critical role of Fe^{4+} species for water oxidation. The newly produced Fe^{4+} without observing quadrupole splitting in the *operando* Mössbauer spectra reflects the relatively regular octahedral geometry of iron atoms (γ-phase NiOOH structure) [41,42]. In particular, one regular FeO_6 octahedron should be surrounded by six regular NiO_6 octahedrons so that the structure can create discrete Fe^{4+} domains within the lattice [16,17,41,43]. All these results are well consistent with the previous DFT studies [16,20]. The abundant high spin Fe^{4+} sites with electrophilicity could provide a more stable environment than Fe^{3+} for the generation of active O intermediates in OER [20,44,45].

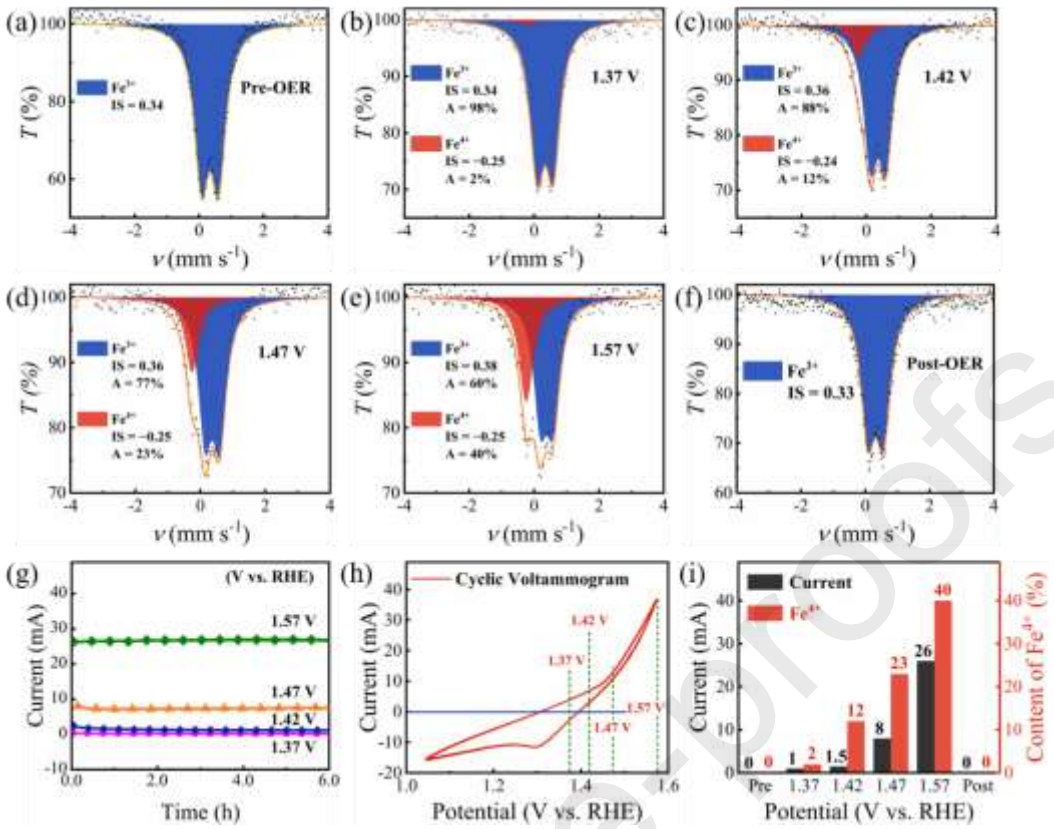

Fig. 4. *Operando* ^{57}Fe Mössbauer spectra of $NiFe_{0.2}$-O_xH_y collected at (a) the open circuit voltage, (b) 1.37 V, (c) 1.42 V, (d) 1.47 V, and (e) 1.57 V (vs. RHE). (f) *Ex-situ* ^{57}Fe Mössbauer spectrum of $NiFe_{0.2}$-O_xH_y collected after OER. The unit of ^{57}Fe Mössbauer parameter of isomer shift (IS) is mm s^{-1}. (g) The current-time curves at different applied potentials obtained during the operando measurements. (h) The cyclic voltammogram without iR correction of $NiFe_{0.2}$-O_xH_y recorded during the operando measurements. (f) The content of Fe^{4+} and corresponding electric current determined at different applied potentials.

4. Conclusions

In conclusion, topotactic transformation was developed as a facile strategy for synthesis $NiFe_m$-O_xH_y. A low overpotential of 263 mV at the current density of 10 mA cm^{-2} and a small Tafel slope of 35 mV dec^{-1} in alkaline condition was achieved. *Operando* Raman results confirmed that the Ni species exist mainly in the form of γ-NiOOH phase structure after electrochemical activation and the transformation from α-

phase to γ-phase is irreversible. In addition, the *in-situ* produced Fe^{4+} with relative content as high as ~40% was observed from *operando* Mössbauer measurement at 1.57 V (vs. RHE). The positive correlation between the Fe^{4+} content and OER current at various applied potentials implies the critical role of *in-situ* produced Fe^{4+} species for catalyzed water oxidation reaction.

Acknowledgments

This work was financially supported by the National Natural Science Foundation of China (21476232, 21961142006), the International Partnership Program of Chinese Academy of Sciences (121421KYSB20170020) and the State Key Laboratory of Catalysis in Dalian Institute of Chemical Physics (N-16-07). Zhichong Kuang thanks the Prof. Bin Liu in Nanyang Technological University for help in electrochemistry testing and the manuscript revision.

References

[1] N.S. Lewis, D.G. Nocera, Proc. Natl. Acad. Sci. U. S. A. 103 (2006) 15729–15735.
[2] M.G. Walter, E.L. Warren, J.R. McKone, S.W. Boettcher, Q.X. Mi, E.A. Santori, N.S. Lewis, Chem. Rev. 110 (2010) 6446–6473.
[3] W.H. Lai, L.F. Zhang, W.B. Hua, S. Indris, Z.C. Yan, Z. Hu, B.W. Zhang, Y.N. Liu, L. Wang, M. Liu, R. Liu, Y.X. Wang, J.Z. Wang, Z.P. Hu, H.K. Liu, S.L. Chou, S.X. Dou, Angew. Chem. Int. Ed. 58 (2019) 11868–11873.
[4] C. Sun, X. Guo, J. Zhang, G. Han, D. Gao, X. Gao, J. Energy Chem. 38 (2019) 34–40.
[5] B.M. Hunter, H.B. Gray, A.M. Müller, Chem. Rev. 116 (2016) 14120–14136.
[6] L. Zhou, M. Shao, M. Wei, X. Duan, J. Energy Chem. 26 (2017) 1094–1106.
[7] C. Tang, H.S. Wang, H.F. Wang, Q. Zhang, G.L. Tian, J.Q. Nie, F. Wei, Adv. Mater. 27 (2015) 4516–4522.
[8] C. Tang, H.F. Wang, X.L. Zhu, B.Q. Li, Q. Zhang, Part. Part. Syst. Charact. 33 (2016) 473–486.
[9] G. Shen, R. Zhang, L. Pan, F. Hou, Y. Zhao, Z. Shen, W. Mi, C. Shi, Q. Wang, X. Zhang, J.J. Zou, Angew. Chem. Int. Ed. 59 (2020) 2313–2317.
[10] K.Y. Zhu, X.F. Zhu, W.S. Yang, Angew. Chem. Int. Ed. 58 (2019) 1252–1265.
[11] W. Zhang, D.H. Li, L.Z. Zhang, X.L. She, D.J. Yang, J. Energy Chem. 39 (2019) 39–53.
[12] X. Deng, J. Huang, H. Wan, F. Chen, Y. Lin, X. Xu, R. Ma, T. Sasaki, J. Energy Chem. 32 (2019) 93–104.
[13] Y. Qin, F. Wang, J. Shang, M. Iqbal, A. Han, X. Sun, H. Xu, J. Liu, J. Energy Chem. 43 (2020) 104–107.
[14] X. Yang, Q.Q. Chen, C. J. Wang, C.C. Hou, Y. Chen, J. Energy Chem. 35 (2019) 197–203.
[15] C. Tang, H.F. Wang, H.S. Wang, F. Wei, Q. Zhang, J. Mater. Chem. A (2016) 3210–3216.
[16] Z.K. Goldsmith, A.K. Harshan, J.B. Gerken, M. Voros, G. Galli, S.S. Stahl, S. Hammes-Schiffer, Proc. Natl. Acad. Sci. U. S. A. 114 (2017) 3050–3055.
[17] J.Y. Chen, L. Dang, H. Liang, W. Bi, J.B. Gerken, S. Jin, E.E. Alp, S.S. Stahl, J. Am. Chem. Soc. 137 (2015) 15090–15093.
[18] H.S. Ahn, A.J. Bard, J. Am. Chem. Soc. 138 (2016) 313–318.
[19] C. Kuai, Y. Zhang, D. Wu, D. Sokaras, L. Mu, S. Spence, D. Nordlund, F. Lin, X.-W. Du, ACS Catal. 9 (2019) 6027–6032.
[20] H. Xiao, H. Shin, W.A. Goddard, 3rd, Proc. Natl. Acad. Sci. U. S. A. 115 (2018) 5872–5877.
[21] X. Li, L. Yuan, J. Wang, L. Jiang, A.I. Rykov, D.L. Nagy, C. Bogdan, M.A. Ahmed, K. Zhu, G. Sun, W. Yang, Nanoscale 8 (2016) 2333–2342.
[22] K. Zhu, H. Liu, M. Li, X. Li, J. Wang, X. Zhu, W. Yang, J. Mater. Chem. A 5 (2017) 7753–7758.
[23] A.I. Rykov, J. Wang, T. Zhang, K. Nomura, Hyperfine Interact. 218 (2012) 139–143.
[24] F. Menil, J. Phys. Chem. Solids 46 (1985) 763–789.

[25] K. Liu, A.I. Rykov, J.H. Wang, T. Zhang, Recent Advances in the Application of Mo beta bauer Spectroscopy in Heterogeneous Catalysis, in: F.C. Jentoft (Ed.) Adv. Catal., Elsevier Academic Press Inc, San Diego, 2015, pp. 1–142.
[26] J.S. Miller, J.L. Manson, Acc. Chem. Res. 34 (2001) 563–570.
[27] P. Gütlich, C. Schröder, V. Schünemann, Spectroscopy Europe 24 (2012) 21–32.
[28] X.N. Li, K.Y. Zhu, J.F. Pang, M. Tian, J.Y. Liu, A.I. Rykov, M.Y. Zheng, X.D. Wang, X.F. Zhu, Y.Q. Huang, B. Liu, J. H. Wang, W.S. Yang, T. Zhang, Appl. Catal. B. 224 (2018) 518–532.
[29] Z. Li, J. Han, L. Fan, R. Guo, Colloid Polym. Sci. 294 (2016) 681–689.
[30] S.J. Gerber, E. Erasmus, Mater. Chem. Phys. 203 (2018) 73–81.
[31] A. Cano, J. Rodríguez-Hernández, L. Reguera, E. Rodríguez-Castellón, E. Reguera, Eur. J. Inorg. Chem. 2019 (2019) 1724–1732.
[32] M. Mullet, V. Khare, C. Ruby, Surf. Interface Anal. 40 (2008) 323–328.
[33] R.P. Gupta, S.K. Sen, Phys. Rev. B 12 (1975) 15–19.
[34] W.E. Buschmann, J.Ensling, P.Gutlich, J.S. Miller, Chem. Eur. J. 5 (1999) 3019–3028.
[35] A. Lisowska-Oleksiak, A.P. Nowak, M. Wilamowska, M. Sikora, W. Szczerba, C. Kapusta, Synth. Met. 160 (2010) 1234–1240.
[36] D.K. Bediako, Y. Surendranath, D.G. Nocera, J. Am. Chem. Soc. 135 (2013) 3662–3674.
[37] M.W. Louie, A.T. Bell, J. Am. Chem. Soc. 135 (2013) 12329–12337.
[38] K.S. Joya, X. Sala, Phys. Chem. Chem. Phys. 17 (2015) 21094–21103.
[39] B.S. Yeo, A.T. Bell, J. Phys. Chem. C 116 (2012) 8394–8400.
[40] F. Dionigi, Z. Zeng, I. Sinev, T. Merzdorf, S. Deshpande, M.B. Lopez, S. Kunze, I. Zegkinoglou, H. Sarodnik, D. Fan, A. Bergmann, J. Drnec, J.F. Araujo, M. Gliech, D. Teschner, J. Zhu, W.X. Li, J. Greeley, B.R. Cuenya, P. Strasser, Nat. Commun. 11 (2020) 2522-2532.
[41] P. Axmann, O. Glemser, J. Alloys Comp. 246 (1997) 232–241.
[42] L. Trotochaud, S.L. Young, J.K. Ranney, S.W. Boettcher, J. Am. Chem. Soc. 136 (2014) 6744–6753
[43] D. Friebel, M.W. Louie, M. Bajdich, K.E. Sanwald, Y. Cai, A.M. Wise, M.J. Cheng, D. Sokaras, T.C. Weng, R. Alonso-Mori, R.C. Davis, J.R. Bargar, J.K. Norskov, A. Nilsson, A.T. Bell, J. Am. Chem. Soc. 137 (2015) 1305–1313.
[44] B.M. Hunter, J.R. Winkler, H.B. Gray, Molecules 23 (2018) 903–910.
[45] H.B. Tao, Y. Xu, X. Huang, J. Chen, L. Pei, J. Zhang, J.G. Chen, B. Liu, Joule 3 (2019) 1498–1509.

Graphical Abstract

Exploring the relationship between high-valent iron content and current intensity of $NiFe_{0.2}$-O_xH_y during oxygen evolution reaction by *operando* ^{57}Fe Mössbauer spectroscopy.